GEORG-AUGUST-UNIVERSITÄT
GÖTTINGEN IN PUBLICA COMMODA SEIT 1737

Fakultät für
Physik [q,p]=iℏ

Bachelor's Thesis

Studium der Top-Quark Polarisation in trileptonischen Endzuständen der tZq-Produktion am ATLAS-Experiment

Studies of the top quark polarisation in trileptonic tZq final states with ATLAS

prepared by

Daniel Werner

from Wuppertal

at the II. Physikalischen Institut

ii

Zusammenfassung

Die *tZq*-Produktion ist eine Unterart der Top-Quark Einzelproduktion im *t*-Kanal, bei der ein zusätzliches *Z*-Boson abgestrahlt wird. Zur Messung der Polarisierung des Top-Quarks, wird dieses aus den Endzustandsteilchen des trileptonischen Zerfalls von *tZq* rekonstruiert. Im Ruhesystem des Top-Quarks kann die Winkelverteilung des Leptons aus dem Top-Quark-Zerfall relativ zum Top-Quark-Spin gemessen werden. Aus dieser Verteilung wird dann per Entfaltung die tatsächliche Verteilung ermittelt. Die Entfaltung hat zum Ziel, die Einflüsse eines Detektors mit begrenzter Auflösung und statistischer Messunsicherheit auf diese Verteilung zu entfernen. Um dies zu erreichen, wird der Effekt des Detektors simuliert, um anschließend die wahre Verteilung der Observable zu finden, die mit der höchsten Wahrscheinlichkeit zur gemessenen Verteilung passt.
Die Rekonstruktion des Top-Quark liefert ein Ergebnis mit hoher statistischer Ungenauigkeit. In einigen Ereignissen ergeben sich Top-Quark-Kandidaten, die nicht mit den echten Top-Quarks des Ereignisses übereinstimmen. Aufgrund dieser fehlerhaft rekonstruierten Top-Quarks ergeben sich weitere hohe Unsicherheiten in der Entfaltung. Insgesamt ist der Entfaltungsprozess in dieser Analyse mit zu hohen Unsicherheiten versehen, um aussagekräftige Ergebnisse aus gemessenen Daten zu erhalten.

Stichwörter: Physik, Bachelorarbeit, Teilchenphysik, Top Quark, Spin-Polarisierung, Entfaltung

Abstract

To find the top quark's polarisation, the top quark is reconstructed from the trileptonic final state. In the top quark's rest frame the angular distribution of the lepton from the top decay with respect to the top spin can be measured. This distribution is then unfolded to find the distribution on truth-level.
Unfolding is a method to find the true distribution of an observable from a distribution as measured in the detector with limited resolution and statistical effects. In the process, the detector effects are simulated to find the truth-distribution with the highest likelihood of being measured as the reconstructed distribution.
The top reconstruction yields top candidates with high uncertainties that often do not match the true top quark in the event. Additional uncertainties arise in the unfolding due to these unmatched top candidates. As a result, the found unfolding procedure does not have sufficient accuracy to get meaningful results from measured data.

Keywords: Physics, Bachelor thesis, Particle physics, Top quark, Spin polarisation, Unfolding

Contents

Contents

1 Introduction

Particle accelerators with changing electromagnetic fields were first realised in 1928 [1] and have been enhanced ever since. The energy per accelerated particle has been increased from 50 keV in 1928 [1] to 6.5 TeV in 2015 [2]. Through the decades of research different elementary particles were discovered and lead to the development of the Standard Model. In 1973 a third generation of quarks consisting of two particles was predicted [3], one of which was the top quark. The top quark was discovered in the CDF and DØ experiments at the TEVATRON in 1995 [4, 5]. Today the energies of accelerators suffice to create all known elementary particles, allowing physicists to study their parameters like mass, lifetime, electric charge, spin, and many more. From comparison of these measured parameters to the values predicted by the Standard Model differences could be found, leading to improved theories to describe particle physics.

As there are still questions in elementary particle physics that cannot be answered by the Standard Model, other theories have been formulated that are usually referred to as Beyond Standard Model (BSM) theories. One possible way of testing the Standard Models predictions and searching for evidence for BSM theories is the measurement of the top quark's polarisation.

1 Introduction

2

2 The Standard Model of Particle Physics

The Standard Model of particle physics is a well established theory to describe elementary particle physics [6]. It contains all known elementary particles and describes three elementary interactions between these particles. Though the Standard Model accurately describes the processes in its field and has successfully predicted the existence of several particles, it is known to be incomplete. Phenomena that cannot be explained by the Standard Model include the observed asymmetry between matter and antimatter in the observable universe [7] and the supposed existence of dark matter that makes up 25 % of the universe's energy [8].

2.1 Elementary Particles

The particles in the Standard Model, as seen in Figure 2.1, are divided into bosons with integer spins and fermions with half-integer spins. The elementary fermions are spin-$\frac{1}{2}$ particles and the bosons are divided into spin-1 gauge bosons and the spin-0 Higgs boson. The gauge bosons are the force carrying particles in the Standard Model with the photon (γ) and gluons (g) being massless particles while the Z and $W^{\pm}$ bosons are massive. The Higgs boson (H) is the only scalar boson and is the excited state of the Higgs field.

The twelve fermions are separated into six quarks and six leptons with three generations each. Their respective charges determine how strongly the fermions couple to the forces explained in section 2.2. In each generation there is an up-type quark (up, charm, top) with electrical charge $+\frac{2}{3}$ e and a down-type quark (down, strange, bottom) with charge $-\frac{1}{3}$ e. Fermions with a weak isospin $I = \frac{1}{2}$ corresponding to negative, or "left-handed", chirality can have the third component of the weak isospin $I_z = \pm\frac{1}{2}$. Those with $I_z = +\frac{1}{2}$ are called up-type fermions, while the other part of the doublet are the down-type fermions with $I_z = -\frac{1}{2}$. Right-handed fermions have an isospin of $I = 0$ and therefore do not form doublets.

Quarks also have a colour charge with the possible values red, green, and blue. Because of

Figure 2.1: The particles of the Standard Model sorted into fermions and bosons. Mass, electric charge, and spin are listed for each particle.

their colour charge, the quarks are subject to the strong interaction that causes them to form composite particles, called hadrons. Based on their spin being integer or half-integer, hadrons are classified into mesons with two quarks, and baryons with three quarks.

Similarly to quarks there are the electron, the muon, and the tau as charged leptons with charge $-1\,\mathrm{e}$ while the matching electron neutrino, muon neutrino, and tau neutrino are electrically neutral. With regard to the third component of the weak isospin the neutrinos are up-type particles and the charged leptons are down type particles with the respective value I_z.

For each particle, the Standard Model also contains its antiparticle with the same mass and lifetime. Other quantities like electric charge and the weak isospin's third component are opposite to the particle's value. Antiquarks carry the anticolours antired, antigreen, and antiblue as colour charges.

2.2 Interactions

The three interactions described by the Standard Model are the electromagnetic, the weak, and the strong force. The electromagnetic force is conveyed by the photon coupling to

electrically charged particles and has an infinite range. The weak and the electromagnetic forces can be combined to the electro-weak interaction, which is mathematically described by the $U(1) \times SU(2)$ symmetry group [9–11]. The four fields arising from these symmetries can be superpositioned to form the exchange particles. These are the massive $W^{\pm}$ and Z bosons, and the massless photon. A particle's coupling to a W boson is essential for particle decay processes and allows quarks to change between the generations. The W boson only couples to left-handed particles, allowing them to change between being up-type and down-type fermions. Weak interactions without a charged current, called neutral current interactions, involve the Z boson, which couples on particles depending on their electric charge and weak isospin. In contrast to the W boson the Z boson couples to both, left-handed and right-handed, particles though the coupling strength is still asymmetric with respect to the particle's isospin. The W boson has a mass of $80.385 \pm 0.015\,\text{GeV}$ [12] and the Z boson's mass is $91.1875 \pm 0.0021\,\text{GeV}$ [13]. Both bosons decay into fermions. The strong interaction's gauge group is $SU(3)$ [14, 15]. The force carrying particles of the strong force are gluons coupling to colour charges. Unlike electrically neutral photons, gluons have a colour charge themselves, allowing them to interact with each other. When quarks move apart from each other, new quark antiquark pairs are created between them, creating new bound states. This effect of quarks not existing as free particles is called confinement [16].

A locally gauge invariant theory of the weak interaction only allows for massless gauge bosons. Thus, the mass of these gauge bosons can only be explained by the Higgs mechanism [17–20]. The mass of the bosons, and in fact also the fermions, is gained by the coupling of the particles to the Higgs field.

2.3 The Top Quark

With a mass of $173.34 \pm 0.27\,(\text{stat}) \pm 0.71\,(\text{syst})\,\text{GeV}$ [21], the top quark is the heaviest particle in the Standard Model. Because of its high mass top quark decays have a large phase space and many decay modes are possible, leading to a large decay width of $1.32\,\text{GeV}$ [22] being predicted by the Standard Model. The top quark's lifetime can be calculated as $\tau = \Gamma^{-1}$ and is therefore very short with about $5 \cdot 10^{-25}\,\text{s}$. The timescale needed for depolarisation of particles is much longer than the time for quarks to hadronise [23], which is in the order of $10^{-23}\,\text{s}$. In summary, the top quark is expected to decay as a single particle before hadronisation and depolarisation of its spin. Therefore, the top quark's spin properties are preserved by its decay products, allowing them to be measured.

Top quark production modes

The top quark can either be produced as a single top quark or as a $t\bar{t}$ pair. For each process the energy in the collision must be at least the top mass or twice the top mass for pair production. The special processes of single top quark production associated with a Z boson and a quark can be categorised as tZq production which contains the processes seen in Figure 2.2. The tZq production can happen as a weak interaction in the t-channel with any of the four participating quarks radiating a Z boson. The Z boson can also be emitted from the W boson propagator in a WWZ vertex. Though it does not contain a Z boson, the non-resonant $\ell^+\ell^-$ production from the W bosons has the same final state as tZq production with a leptonically decaying Z boson and is therefore classified as a contribution to tZq production too [24, 25].
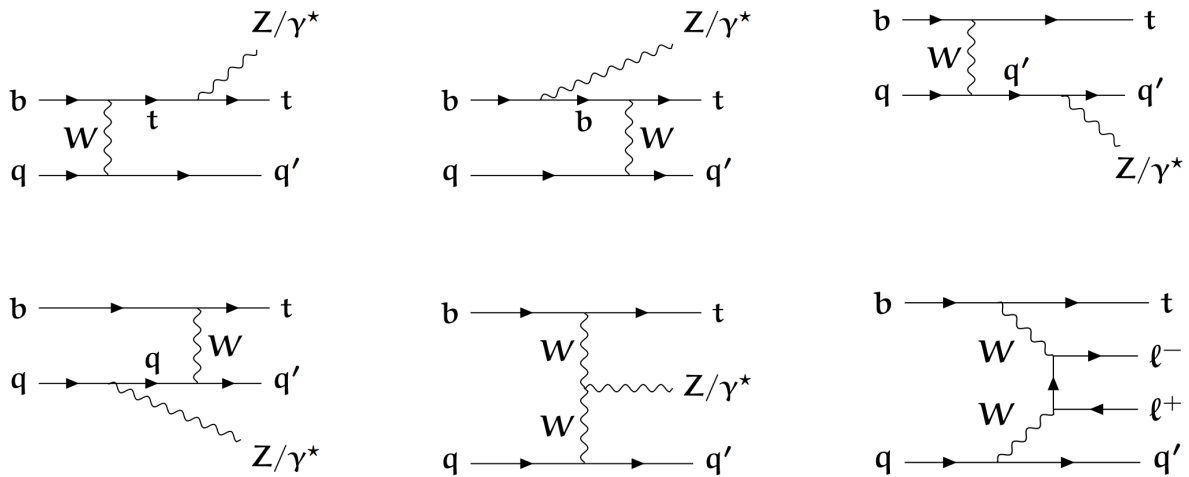

Figure 2.2: Contributions to tZq production via Z radiation in a weak t-channel single top production (in the three upper and the lower left diagrams), triple gauge boson coupling WWZ (in the lower mid diagram), and via non-resonant $\ell^+\ell^-$ production (in the lower right diagram).

Since the valence quarks of a proton-proton collision do not contain any bottom quarks, a possible origin of the bottom quark in the initial state is a quark-antiquark production from a gluon as can be seen in Figure 2.3.

Top quark decay modes

The top quark has a mass greater than the combined mass of a W boson and any other quark, allowing it to decay into an on-shell W^+ boson and a down-type quark. The cross-sections for decays into the different down-type quarks are affected by the Cabibbo-Kobayashi-Maskawa-Matrix (CKM-Matrix, V_{CKM}) [3]. Since the element $|V_{tb}|$ for changes
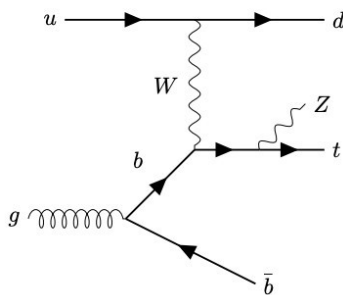
Figure 2.3: A *tZq* production feynman diagram with a the *b* quark originating in a quark-antiquark production by a gluon. The final state has a $\bar{b}$ spectator quark.

between top and bottom quarks is almost unity and $|V_{tb}| \gg |V_{td}|, |V_{ts}|$, the resulting branching ratio for a bottom quark is nearly 100 % (101.4 % $\pm$ 3.2 % (syst)) [26]. Therefore, a *b*-jet can be measured in almost all top quark decays. The W^+ boson can either decay into a charged antilepton (e^+, μ^+, τ^+) and the corresponding neutrino $(\nu_e, \nu_\mu, \nu_\tau)$ or into a $q'\bar{q}$ pair. The branching ratios for the W boson according to [27] can be seen in Figure 2.4. In the case of a $q\bar{q}$ pair being created, these quarks form jets that can be detected. When the W^+ boson decays into a positron or an antimuon the relevant antilepton can be observed together with missing transverse energy from the neutrino that cannot be observed. An antitau is too short-lived to reach the detector and only its decay products can be measured. These products are always a tau antineutrino and either up to four mesons, or a lighter antilepton and its neutrino.

To predict possible particle combinations that can be measured in the detector after *tZq* production, the *Z* boson and the additional quark must be considered too. The *Z* boson decay's branching ratios measured by [13] are included in Figure 2.4. The possible decay products are a $q\bar{q}$ pair, an $\ell^+\ell^-$ pair, or a third product that is invisible to the detector. With the Standard Model prediction that these invisible decay products are $\nu\bar{\nu}$ pairs the number of neutrino generations can be measured to be 2.9840 ± 0.0082 [13]. In the detector the signal from the *Z* boson is therefore either two jets, two charged leptons, or just missing transverse energy, if the decay products are neutrinos. The quark from the *tZq* production is detectable as a single jet.

Top quark spin polarisation

A particle's polarisation describes whether the spin direction is equally distributed over all possible directions or whether there is a preferred direction which would be called the polarisation direction. The fraction of spin that is parallel to the direction of momentum
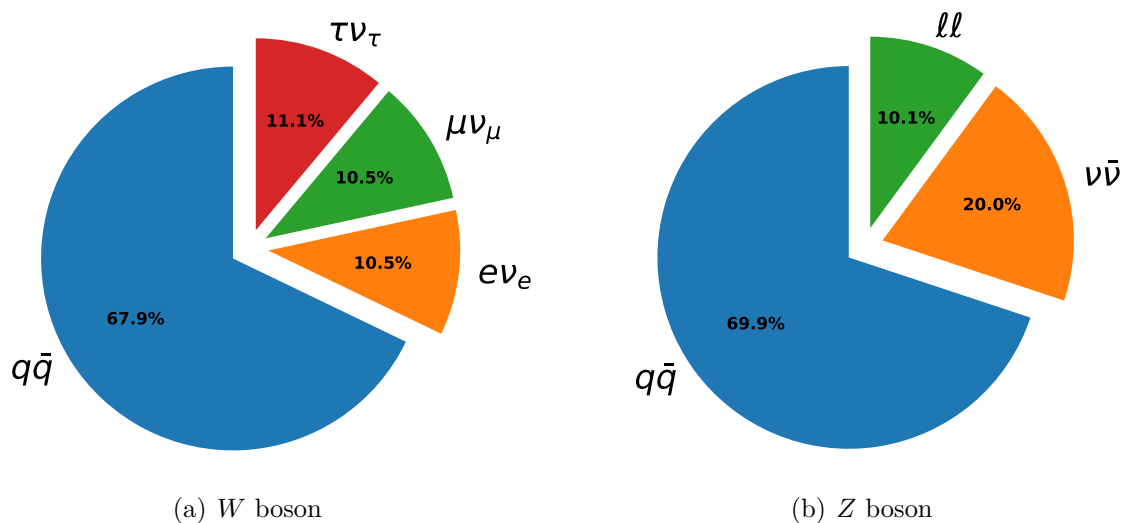
(a) *W* boson   (b) *Z* boson

Figure 2.4: Branching ratios for the decay of (diagram a) a *W* boson according to [27] and (diagram b) a *Z* boson according to [13].

of a particle is called the helicity of the particle. In the limit of a massless particle the helicity becomes equivalent to the chirality of the particle. Since *W* bosons only interact with particles with a left-handed chirality, the initial quarks *b* and *q* must be left-handed. The top quark is then expected to be polarised in the direction of momentum of the final state quark q' [28]. When the top quark decays via the *W*-boson into a lepton, this lepton's direction of momentum is correlated with the polarisation with the angular correlation α_ℓ. [29]. Measurement of the polarisation can be carried out via reconstructing the angle θ^* between the q' and the lepton in the top quark's rest frame. The differential cross section over this angle can be fitted to the expected formula to find the polarisation $P_t^{(q')}$ and the spin asymmetry defined as $A_t = \frac{1}{2} P_t^{(q')} \alpha_\ell$:

$$\frac{\mathrm{d}\sigma}{\mathrm{d}\cos(\theta^*)} = \frac{\sigma}{2}\left(1 + P_t^{(q')}\alpha_\ell \cos(\theta^*)\right) = \sigma\left(\frac{1}{2} + A_t \cos(\theta^*)\right). \quad (2.1)$$

With *tZq* production multiple couplings of the SM can be probed. As seen in the first diagram of Figure 2.2 and in Figure 2.3, the top quark can radiate a *Z* boson before decaying. Through this coupling the electro-weak sector of the top quark can be studied. Another possible interaction that can be probed, is the triple gauge coupling between the *W*- and the *Z* boson as seen in the fifth diagram of Figure 2.2.

In conclusion, the top polarisation is sensitive to changes in different couplings, which can be studied in an effective field theory approach.

3 The Experimental Setup

3.1 The Large Hadron Collider

The Large Hadron Collider (LHC) [30] is a circular particle accelerator with a length of 27 km. It collides two beams of high energy proton bunches at the four positions on the ring where the detectors ALICE [31], ATLAS [32], CMS [33], and LHCb [34] are located. Bunch crossings in the LHC happen every 25 ns with an average 27 collisions per bunch crossing [2]. The centre-of-mass energy reached in 2015 was $\sqrt{s} = 13$ TeV. This energy suffices to investigate nearly all possible interactions within the Standard Model and a lot of possible BSM scenarios.

3.2 The ATLAS Detector

With the high frequency at which the protons collide, and the high energies allowing for many particles to be created, detectors need to effectively decide, which events to record, and they need to accurately identify the created particles. The decision which events to record is made by a hardware based first level trigger and software based high level triggers [35]. The level 1 trigger determines a region of interest for further analysis, and rejects events without high p_T-objects. At the higher level triggers the objects from the event are reconstructed within the region of interest to reject events with a low resolution or if the reconstruction is not possible. The remaining objects after these selections are fully reconstructed and stored for later analysis. To identify different particles and measure their energy, momentum, and trajectory, detectors consist of different layers, in which the particles interact differently with the matter of the detector. Important criteria for the order of the layers are the spatial resolution of a detector, the cost to build it in the required size, and whether particles pass through it to be detected by later detector layers. The design of the ATLAS detector can be seen in Figure 3.1. The innermost layers of the ATLAS detector are a pixel detector and a semiconductor tracker [32] both made up of small silicon semiconductor sensors [36], in which charged particles create a signal by ionising the material. This detector is followed by a transition radiation tracker [32]
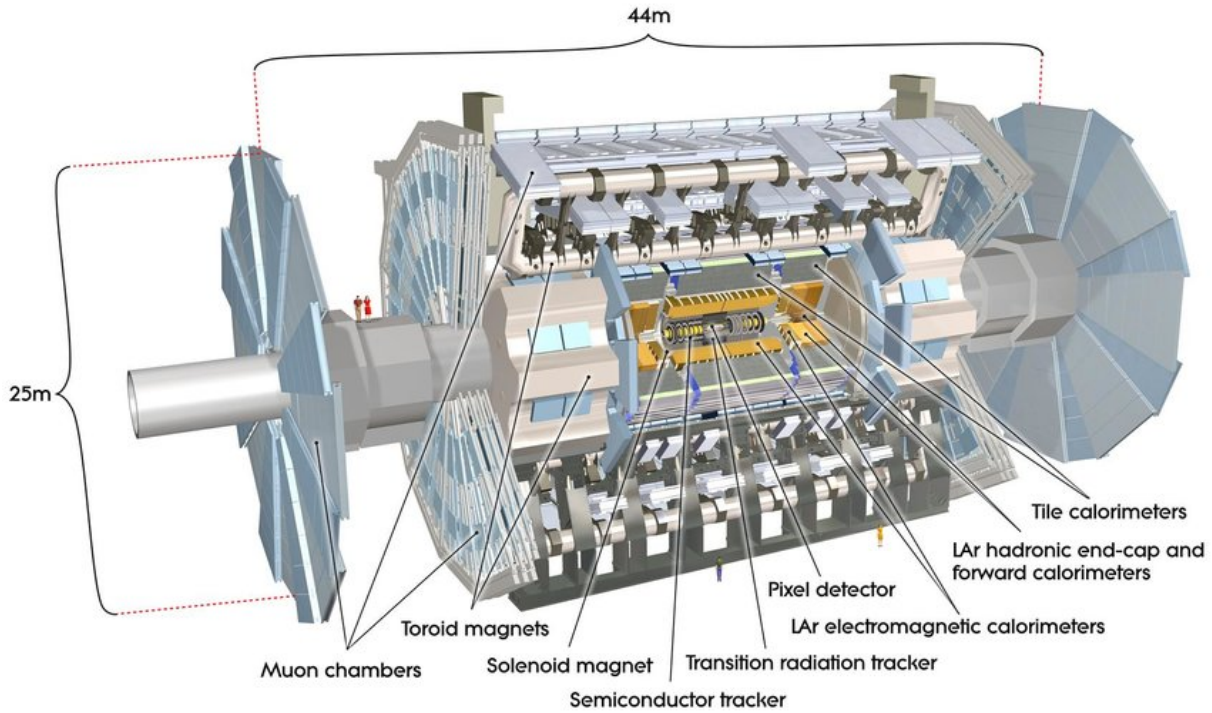
Figure 3.1: Design of the ATLAS detector with its different detector layers.
ATLAS Experiment © 2008 CERN.

that is based on the ionisation of gas in drift chambers, where the ions and electrons are measured by wires with a high voltage. The used gas mixture is Xenon (70%), CO_2 (20%), and CF_4 (10%) [36]. Between the drift chambers are materials with different refractive indices to cause relativistic particles to radiate photons when passing through the boundaries between the materials. The combination of several layers of these small pixels, strips, and drift chambers can measure a three-dimensional track of the particles with decreasing resolution towards the outside of the detector. The resolution perpendicular to the beam direction is $\sigma = 12\,\mu$m for the pixel detector, $16\,\mu$m for the silicon strips, and $170\,\mu$m for the transition radiation tracker [36]. The solenoid magnet outside these detector layers creates a magnetic field parallel to the beam line. In this field particles moving in transverse direction to the beam line are deflected. The curvature of the particles' trajectories is used to measure their momenta. The emitted transition radiation then allows to distinguish light particles that are more relativistic than heavy particles of the same momentum.

Outside the Inner Detector are an electromagnetic and a hadronic calorimeter for measuring the energy of the particles. Inside the calorimeter electrons create photons through Bremsstrahlung and photons create electrons and positrons through pair production. The

initial particle's energy is distributed among these secondary particles. Hadrons can create electrons, photons, and other hadrons through strong interactions with atomic nucleons in matter. The energy depositions of the shower particles are measured individually and combined by jet reconstruction algorithms into groups which are called jets. Through this combination of the energy deposits, the energy of the jet and thus the energy of the primary parton is determined. The electromagnetic calorimeter is made up of Lead for shower creation and liquid Argon for the detection of showers [36]. Similarly, the hadronic calorimeter uses steel as an absorbing material and scintillating tiles as an active medium [36].

The outermost part of the ATLAS detector is the muon spectrometer. It works similarly to the Inner Detector by measuring the muons trajectories in a gas mixture of Argon (93%) and CO_2 (7%) with a resolution of $80\,\mu$m [36] to measure their momentum.

At each end of the detector there is an end cap consisting of calorimeters, toroid magnets, and muon chambers to detect particles emitted at small angels with respect to the beam line.

4 Object reconstruction

4.1 Monte Carlo generators

To investigate the effect of the detector on an observable, and to study the efficiency of event selection and reconstruction, data samples cannot be used, since the true reactions and final states are not known. For those purposes the events can be simulated by specifically created Monte Carlo generators. Those are based on standard model calculations to find probabilities for different reactions and then simulate the collisions. The information generated this way is called the truth-level information since it contains the particles' true quantities and information on their respective creation. Additional simulations are performed to include the detector measuring the particles of the truth-level events. This process adds statistical uncertainties to the particles' quantities and can potentially misidentify the particles. The resulting samples contain the reconstruction-level (short reco-level) information in the same format as given from the detector after measuring real events. To simulate the events that are studied in this analysis, the general purpose Monte Carlo generator PYTHIA [37] is used in combination with aMC@NLO [38] to account for QCD corrections. For the b quarks involved in the process, the 4 flavour scheme (4FS) was used by not considering b quarks as partons in the proton. Instead, the b quarks were generated using massive QCD splitting functions.

4.2 Objects

In the detector, an electron is reconstructed from the combination of an energy deposition in the calorimeter that matches a reconstructed track in the Inner Detector [39]. Electrons with a high pseudorapidity have reduced resolution in the Inner Detector and deposit their energy in the endcap calorimeter, which is less efficient than the barrel calorimeter. Similarly, electrons with a pseudorapidity between 1.37 and 1.52 pass through the gap between the barrel detectors and the endcap detectors. They traverse part of the detector's support structure, which is inactive material and greatly reduces the resolution of the energy measurement. In combination, electrons are only reconstructed for $|\eta| < 1.37$ or

$1.52 < |\eta| < 2.5$.

The identification of electrons is improved by using the tight likelihood working point with an average efficiency of 80% [39].

Since non-prompt electrons can emerge from decays of other particles after the original collision, the reconstructed electrons should be isolated to avoid misidentifying the non-prompt electrons as prompt. The isolation criteria are based on measuring the deposited energy in a cone of $\Delta R = 0.2$ around the electron. For the isolation in the Inner Detector the cone size can be smaller for high p_T values by taking $\Delta R = \min(\frac{10\,\text{GeV}}{p_T}, 0.2)$. This accounts for electrons from high p_T particle decays to be close to the other decay products. The isolation is determined with the loose working point by requiring the deposited energy in the cone in the calorimeter to be below 20% of the electron's p_T. For the energy measured in the variable sized cone in the Inner Detector, the relative energy must be below 15% [39].

Muons can be detected in the Inner Detector as tracks, but only deposit a negligible amount of energy in the calorimeters as they are minimum-ionising particles (MIPs). Therefore, muons can pass through both calorimeters and can then be detected in the muon spectrometer. If a track found in the muon spectrometer can be matched to a track in the Inner Detector, the corresponding particle is identified as a muon [40]. Since a measured track in the Inner Detector is necessary for this identification, the muon is only reconstructed for $|\eta| < 2.5$, similarly to the electrons. To extend this geometrical limit up to $|\eta| < 2.7$, tracks in the muon spectrometer without an associated track in the Inner Detector are identified as muons as well.

For the muon identification, the medium working point is used, which considers mainly muons from combined tracks in Inner Detector and muon spectrometer. Muons with hits only in the muon spectrometer are only considered if they are in the region $2.5 < |\eta| < 2.7$ [40].

To determine whether a muon is isolated, the loose working point is used, similar to the electron isolation. The cone for the calorimeter deposits is the same as for the electron, while the variable cone in the Inner Detector has a maximum size of 0.3. In $Z \to \mu\mu$ processes this working point has an efficiency of 99% [40].

Jets are reconstructed from energy deposited in adjacent calorimeter cells. The grouping of the energy clusters into jets is achieved using the anti-k_t algorithm [41]. Jets do not need to be matched to tracks in the Inner Detector and can be reconstructed with high pseudorapidities $|\eta| < 4.5$.

The hadrons formed by bottom quarks have comparatively high lifetimes since they only decay via the weak interaction. Due to these lifetimes, they can travel distances of up to

several millimetres away from the collision point before decaying in a secondary vertex. The jets originating from bottom quarks (*b*-jets) are characterised by originating in such secondary vertices. To identify a jet as a *b*-jet, tracks in the Inner Detector are needed to determine the secondary vertex. Due to the needed tracking resolution, these jets must satisfy $|\eta| < 2.5$. The *b*-tagging algorithm DL1r used in this thesis is based on a deep neural network [42].

In the ATLAS detector there are usually multiple scattering processes per bunch crossing resulting in energy deposits from the different events occurring at the same time. This effect is referred to as in-time pileup. Additionally, out-of-time pileup is found when remnants of previous processes are still being detected. To differentiate between these pileups and jets, the jet-vertex-tagger (JVT) can be used to tag and reject pileup jets [43]. The JVT is based on reconstructing the primary vertices, from which jets originate, to discriminate between pileup and signal jets. For this reconstruction tracks in the Inner Detector are necessary limiting the use of the JVT to object with $|\eta| < 2.5$. To reject jets with $2.5 < |\eta| < 4.5$, the forward jet-vertex-tagger (fJVT) algorithm is used [44].

Neutrinos are not measured in any part of the ATLAS detector due to their negligible interaction cross section with matter. The only trace of a neutrino being involved in a particle reaction is therefore the absence of its energy and momentum in the transverse plane. Since the colliding particles in the collider have no momentum transverse to the beam line, the total transverse momentum of the final state should be zero through the conservation of momentum. The negative sum of all measured transverse momentum vectors is interpreted as the missing transverse momentum vector or missing transverse energy (E_T^{miss}) [45].

4 Object reconstruction

5 Event Selection and Reconstruction

The studied events are expected to contain the associated quark q' of the top production, the decay products from the Z boson, and the decay products from the top quark itself. Additional jets can contribute through final state QCD radiation. To not exclude this case, both final states with and without an additional untagged jet are selected for the analysis.

The quark q' will be measured as an untagged jet. From the Z's decay products, the $\ell^+\ell^-$ pair is used for this analysis due to the clean event signature in the hadronic environment of the LHC. Since Z interactions do not allow flavour changes, the leptons are expected to have the same flavour while also being oppositely charged. Such $\ell^+\ell^-$ pairs are also known as opposite-sign, same-flavour (OSSF) pairs.

The decay mode of the top quark considered for this analysis is the decay into a bottom quark and a W boson. This boson decays leptonically into a charged electron or muon, and the corresponding neutrino. The reaction can therefore be summarised to:

$$pp \to b\,q \to t\,Z\,q \to q\,b\,\ell\,\ell^+\ell^-\,\nu \tag{5.1}$$

5.1 Cuts

To account for low energetic backgrounds, it is useful to require a minimum p_{T} of all detected objects [39, 40].

The p_{T} required for all leptons is $20\,\mathrm{GeV}$ [24] while they must also satisfy $|\eta| < 2.5$. Since the first level trigger of the detector only saves events with high-p_{T} particles, at least one of the leptons is required to have a p_{T} of at least $28\,\mathrm{GeV}$. The required p_{T} for the measured jets is $35\,\mathrm{GeV}$ [24] while for b-jets $|\eta| < 2.5$ is required and $|\eta| < 4.5$ for untagged jets. As two of the leptons originate from the Z boson, an OSSF pair is expected among the three leptons that can be reconstructed to a Z candidate with $|m_{\ell\ell} - m_Z| < 10\,\mathrm{GeV}$. The reconstruction is described in the following section.

5.2 *Z* boson reconstruction

To reconstruct the *Z* boson candidate from the available leptons, first all OSSF pairs are identified. For each pair the four-momenta are added to find the four-momentum of the *Z* candidate. Out of all OSSF pairs, the one with the invariant mass $m_{\ell\ell}$ closest to the *Z* boson's mass of $91.1875 \pm 0.0021\,\mathrm{GeV}$ [13] is considered to originate from the *Z* decay. The remaining lepton is associated with the decay of the top quark.

5.3 Top decay angle reconstruction

The lepton from the top decay is used to reconstruct the *W* boson. Since the missing transverse energy can be measured and the neutrino's mass can be neglected, only the neutrino's momentum along the beam axis is left unknown. As the minimum required energy of the lepton of $20\,\mathrm{GeV}$ is much higher, than the mass of either an electron or a muon, those can be neglected as well. The invariant mass of the *W* boson can be rearranged into the quadratic equation (5.2) with the coefficients in (5.3).

$$m_W^2 = \left(p_\nu^\kappa + p_\ell^\lambda\right)^2 \approx 2p_\nu p_\ell \Leftrightarrow a \cdot p_{z,\nu}^2 + b \cdot p_{z,\nu} + c = 0 \tag{5.2}$$

$$
\begin{aligned}
a &= p_{z,\ell}^2 - E_\ell^2 \;, \\
b &= 2\,p_{z,\ell}\left(\frac{1}{2}m_W^2 + \vec{p}_{T,\ell} \cdot \vec{p}_{T,\mathrm{miss}}\right) \;, \\
c &= \left(\frac{1}{2}m_W^2 + \vec{p}_{T,\ell} \cdot \vec{p}_{T,\mathrm{miss}}\right)^2 - E_\ell^2\,\vec{p}_{T,\mathrm{miss}}^2 \;.
\end{aligned}
\tag{5.3}
$$

Of the two possible momenta of the neutrino along the beam line, the smaller one is kept to reconstruct the *W* boson. In case of complex solutions only the real part is used as a unique solution.

With the reconstructed *W* boson and the *b*-jet, the top quark can be reconstructed by adding the four-momenta. The top quark's polarisation is known to be parallel to the direction of q' in the top quark's rest frame. Therefore, both the q' jet and the lepton from the *W* decay are boosted into the top rest frame since all particles' four-momenta can be reconstructed. In case of two untagged jets being detected, the one with higher p_T is assumed to be corresponding to the quark q'. The angle θ^* is defined to be between the lepton and the quark. The cosine of this angle $\cos(\theta^*)$ is the observable of interest to study the top quark's polarisation in comparison to equation (2.1).

6 Unfolding

Unfolding is a method used on measured distributions to reconstruct the truth-distribution. To find an unfolding process, simulated distributions must be used to know the truth-distribution and the result simultaneously. The effects of the detector can be mathematically described by the migration matrix M, the acceptance A and the efficiency ϵ. Each column of the migration matrix corresponds to one bin of the truth-distribution, while each row is associated with a bin of the reconstructed distributions. Thus, the matrix element M_{ij} gives the proportion of events in the truth-bin with index i that are measured to be in the bin with index j in the reconstructed distribution.

The efficiency of a bin i gives the percentage of events in this bin in the truth-distribution that are included anywhere in the reco-distribution. In contrast, the acceptance is defined as the percentage of events in a reco-bin j that belong to the same bin in the truth-distribution. The efficiency accounts for events that are missed by the detector or rejected by the cuts, while the acceptance takes events from background processes into account that are identified as events from the signal. The migration matrix contains the information on events that are measured to be in a different bin in the reconstructed distribution, compared to the true distribution. The whole effect of the measurement can be described by the response matrix as a combination of the three effects. To calculate an element of the response matrix, the migration, efficiency and acceptance must be combined according to equation (6.1) [46]:

$$R_{ij} = \epsilon_i M_{ij} \frac{1}{A_j} \tag{6.1}$$

6.1 Profile Likelihood Unfolding

In the profile likelihood unfolding, each line of the response matrix is considered as the reco-distribution if only events in the corresponding truth-bin are measured. These distributions can be added while each is scaled by the number of events in the truth-bin to form a measured distribution. The scaling factors of each bin are used as free parameters $\mu_{i=0,\dots,N}$. By performing a fit to match the weighted sum of the distributions to a given

data distribution, the parameters μ_i are computed. That way the truth-distribution is determined from the measured data distribution.

Since the response matrix is computed from simulated events, it is affected by the systematic uncertainties of the used Monte Carlo generators and the detector. These uncertainties are included as nuisance parameters θ_j in the distribution. To fit the free parameters to the data distribution, a likelihood function $\mathcal{L}$ is maximised. In equation (6.2) the likelihood to measure a distribution $\vec{n}$ is defined. The parameter μ_i can be interpreted as the expectation value of bin i and n_i as the measured content in bin i. The n_i are Poisson-distributed, while the uncertainties are normally distributed. This normal distribution is characterised by the expectation values θ_j^0 and standard deviations $\Delta\theta_j$.

$$\mathcal{L}\left(\vec{n}|\vec{\mu},\vec{\theta}\right) = \prod_{i\in\text{bins}} \frac{\mu_i^{n_i}}{n_i!}\exp(-\mu_i) \cdot \prod_{j\in\text{syst.}} \exp\left(-\frac{\left(\theta_j - \theta_j^0\right)^2}{4(\Delta\theta_j)^2}\right) \tag{6.2}$$

For any given choice of $\vec{\mu}$, the profile likelihood is defined in (6.3) as the maximum value of the likelihood. The profile likelihood is only dependant on μ. Working with the profile likelihood allows to include the uncertainties in the fit without needing more parameters. To simplify the fit numerically, $t(\vec{\mu})$ is defined from the normalised profile likelihood $\lambda(\vec{\mu})$ according to equation (6.4).

$$\mathcal{L}_{\text{profile}}\left(\vec{n}|\vec{\mu}\right) = \max\left\{\mathcal{L}\left(\vec{n}|\vec{\mu},\vec{\theta}\right)\Big|\vec{\mu} = \text{const}\right\} \tag{6.3}$$

$$\Rightarrow \lambda\left(\vec{n}|\vec{\mu}\right) := \frac{\mathcal{L}_{\text{profile}}\left(\vec{n}|\vec{\mu}\right)}{\max\left\{\mathcal{L}\left(\vec{n}|\vec{\mu},\vec{\theta}\right)\right\}}$$

$$\Rightarrow t\left(\vec{n}|\vec{\mu}\right) = -2\log\left(\lambda\left(\vec{n}|\vec{\mu}\right)\right) . \tag{6.4}$$

For processes with a large migration between neighbouring bins, the unfolding can lead to a result strongly different from the truth-distribution due to statistical fluctuations in the reco-distribution. An adjustment to the unfolding can be made by including more terms in the likelihood from equation (6.2). This adjustment is called regularisation and a typical constraint is that each bin's content is normal distributed as seen in equation 6.5. The regularisation strength τ determines the regularisation effect with no regularisation at $\tau = 0$ and a strong regularisation at higher τ.

$$\mathcal{L}_{\text{reg}}\left(\vec{n}|\vec{\mu},\vec{\theta}\right) = \mathcal{L}\left(\vec{n}|\vec{\mu},\vec{\theta}\right) \cdot \prod_{i\in\text{bins}} \exp\left(-\frac{\tau^2}{2}(\mu_i - n_i)^2\right) \tag{6.5}$$

7 Analysis

7.1 Data vs. MC / Background examination

To examine the applied cuts, they can be applied to both signal and background processes and to measured data. The result can be drawn as a stacked histogram of the signal and background processes and the data events as a point for each bin. As an example, this plot is performed for the distributions of the transverse momentum for different particles. The leading and sub-leading leptons and jets are used as particles that do not require further reconstruction from the information given by the detector. To obtain a good resolution of the distribution, while not having bins with too little content, the bins are chosen to be larger in regions with less events. The smallest bin limit is for each object chosen according to the applied p_T cut. That way, the distributions start at $28\,\text{GeV}$ for the leading lepton, at $20\,\text{GeV}$ for the sub-leading one, and at $35\,\text{GeV}$ for both jets. A comparison of signal and background to the data can be seen in Figures 7.1 and 7.2.
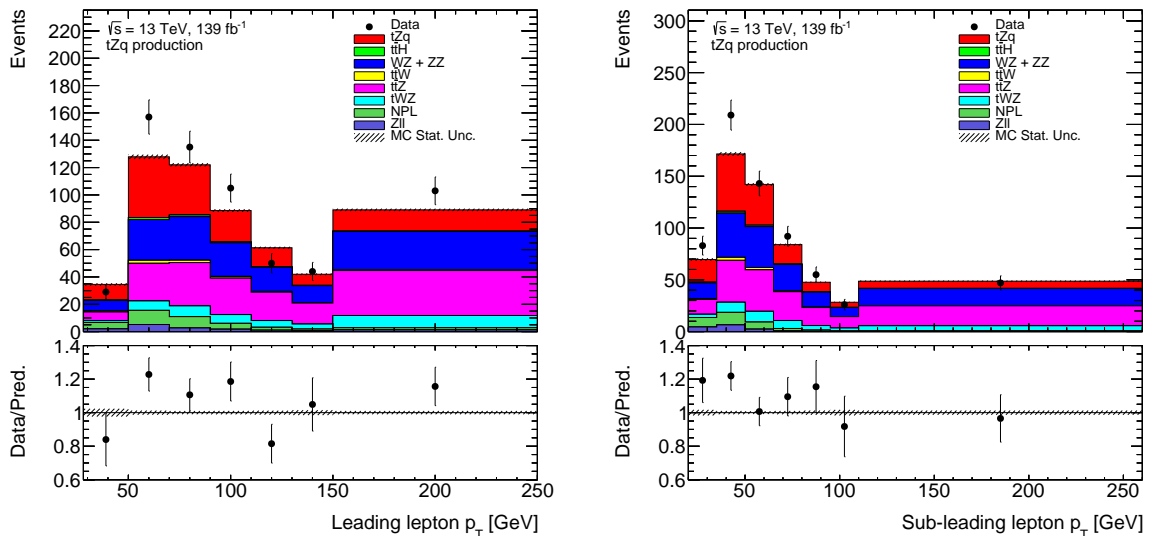
Figure 7.1: Transverse momentum of the (a) leading and (b) sub-leading lepton. Contributions from the tZq signal and backgrounds in a stacked histogram and the data measured in Run 2 as one point per bin. In the ratio plot the ratio between the data points and the histogram is plotted for each bin.
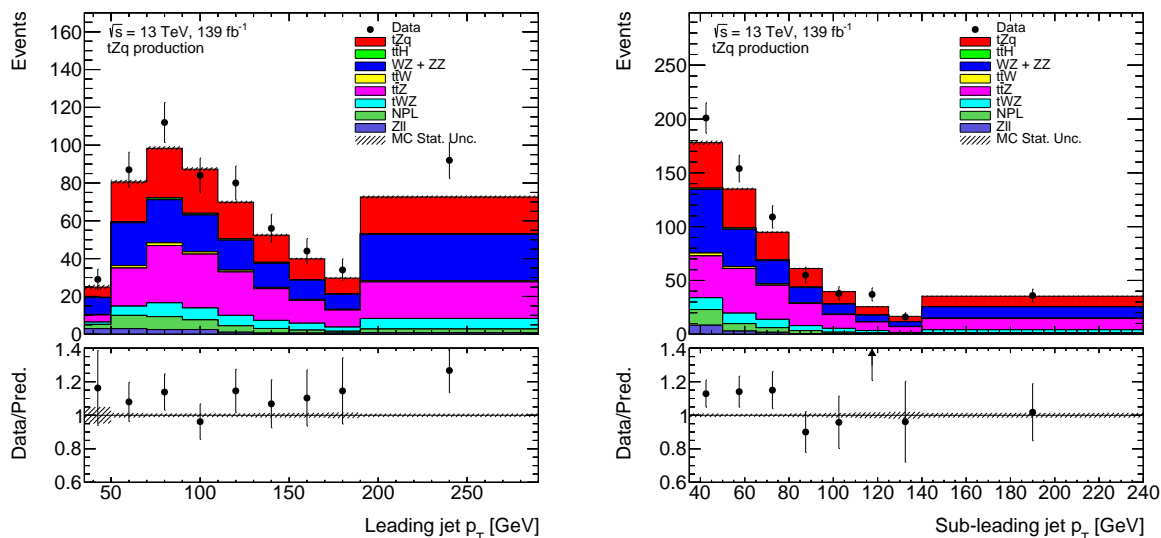
Figure 7.2: Transverse momentum of the (a) leading and (b) sub-leading jet. Contributions from the tZq signal and backgrounds in a stacked histogram and the data measured in Run 2 as one point per bin. In the ratio plot the ratio between the data points and the histogram is plotted for each bin.

In these histograms, the simulated events must be weighted to be comparable to the data measured in the LHC Run 2. The weights from the Monte Carlo generator are multiplied with the integrated luminosity of $139\,\mathrm{fb}^{-1}$. An overview of the considered processes is given in Table 7.1 with the number of found events in each process.

The comparison between the leading and the sub-leading lepton shows a wider distribution for the leading lepton with more events with high p_T objects. This fits the expectation since in each event individually the leading lepton must have a higher p_T than the sub-leading one. In the same way, the distribution of the leading jet is wider and reaches its maximum at a higher p_T of around $80\,\mathrm{GeV}$, compared to $40\,\mathrm{GeV}$ for the sub-leading jet. This behaviour is similar for all contributing processes with small changes in the width and maximum of each distribution. The most notable exception are the non-prompt leptons that show a strong preference for low p_T values.

In most bins, the Monte Carlo generated distribution is within two standard deviations of the data points as can be seen from the ratio plots. Therefore, the data and Monte Carlo distributions are in agreement. From the events per production mode in Table 7.1, it is evident that the most important background processes are diboson (WZ and ZZ) and $t\bar{t}Z$ production with similar yields to tZq production. The tWZ production, $Z\ell\ell$ production and non-prompt lepton (NPL) can also be seen in the stacked histograms, while $t\bar{t}W$ and $t\bar{t}H$ are almost negligible as they each account for approximately one percent of the total events.

Process	Number of events
tZq	156.42
$t\bar{t}H$	5.04
$WZ + ZZ$	162.75
$t\bar{t}W$	7.77
$t\bar{t}Z$	170.69
tWZ	43.20
NPL	32.44
$Z\ell\ell$	14.96
Sum without Data	539.3
Data	655

Table 7.1: Number of total events per signal and background contribution and for the measured data.

7.2 Top Reconstruction

After reconstructing the top quark, its mass can be calculated and saved as a histogram. The top reconstruction at reco-level is done as described in Section 5.3. At truth-level, the top quark's properties are known, allowing to directly calculate the mass. Again, the bins around the expected top mass are smaller, since the distribution is expected to have a narrow peak there. By dividing the bin contents of the distribution by the integrated luminosity, the contents are converted from numbers of events into the cross section. A division by the respective bin width computes the differential cross section $\frac{\mathrm{d}\sigma}{\mathrm{d}m_t}$ from the bins with the unit $\mathrm{fb\,GeV^{-1}}$. In Figure 7.3 (a), the distribution can be seen to be narrow as expected from the SM. The reconstructed mass follows a much wider distribution, as seen in Figure 7.3 (b). The distribution of the reconstructed top, noticeably, has a long tail of candidates with much higher masses than the actual known mass of top quark of approximately $173\,\mathrm{GeV}$ [21]. Since the reconstruction differs so strongly from the expectation, there seems to be some larger source of uncertainty in the reconstruction. To search for the source of such inaccuracies, the Z boson reconstruction was investigated by checking, whether the leptons of the OSSF pair are within a $\Delta R = 0.1$ cone of the truth-level leptons. It was found that in around 86% of the matched entries the OSSF pair was correctly identified. This leads to a wrongly reconstructed W boson in the other 14% of events, since the wrong lepton is associated with the top decay. Further analysis is needed to improve the reconstruction and possibly isolate other variables that cause
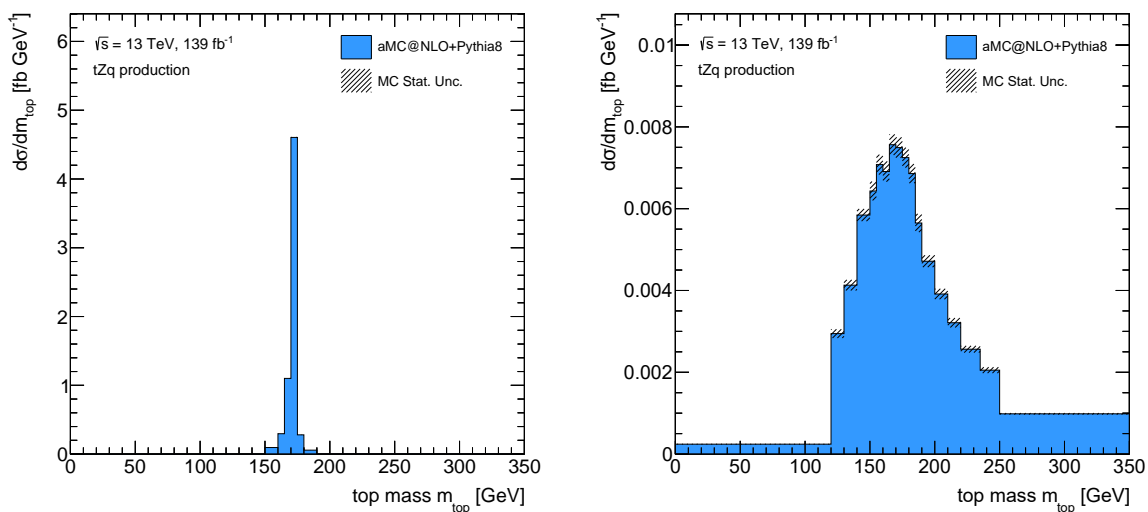
Figure 7.3: Differential cross section of *tZq* production with respect to the invariant mass of the top quark. Calculated on (a) truth-level and on (b) reco-level with a top quark reconstruction as described in Chapter 5.

the uncertainty. One possibility are missing transverse energy values that are measured to high. This happens if any object in the detector is missed or attributed to a wrong primary vertex.

7.3 Top Polarisation Reconstruction

The polarisation observable $\cos(\theta^*)$ can be computed from the reconstructed top quark in the samples from both the true, and the reconstructed events. As with the top mass, the distribution of events can be converted into a differential cross section. The differential cross section over $\cos(\theta^*)$ on both truth- and reco-level is shown in Figure 7.4. In the truth-distribution the linear dependency, described by the equation (2.1), can clearly be seen. The reconstructed distribution only roughly follows a linear function in the middle of the distribution. For high $\cos(\theta^*)$ the bins are much lower than expected by the slope. In this region the angle between the lepton from the top decay and the jet from the quark q' is close to zero with the particles moving almost parallel. In the detector, such events look similar to non-prompt leptons, and have a high risk of being rejected by the isolation criteria. For these distributions, the efficiency and the acceptance can be calculated to describe the detector's effect on the observable. These quantities are shown in Figure 7.5.
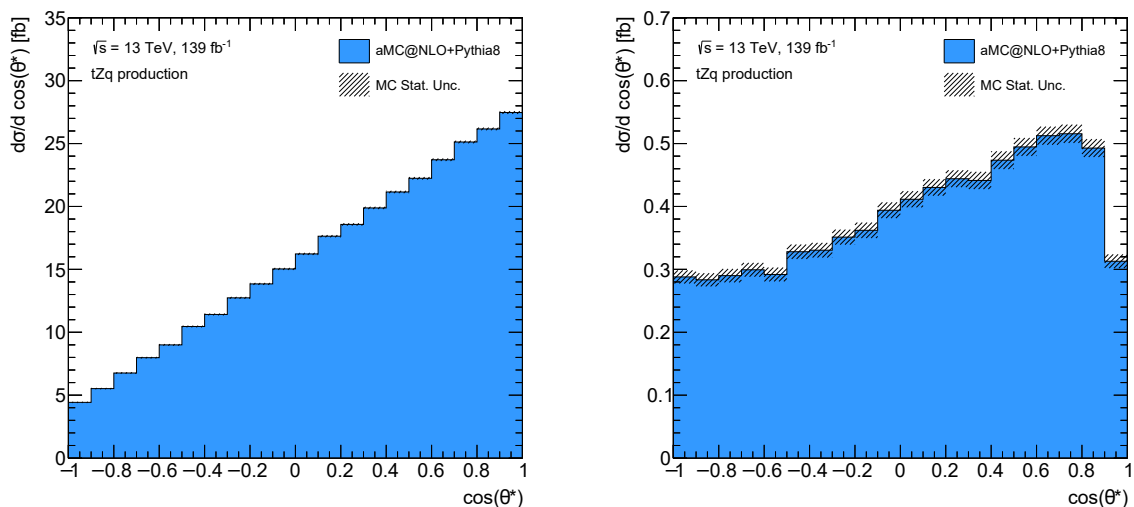
Figure 7.4: Differential cross section with respect to the top polarisation observable $\cos(\theta^*)$ on (a) truth- and (b) reconstructed level.
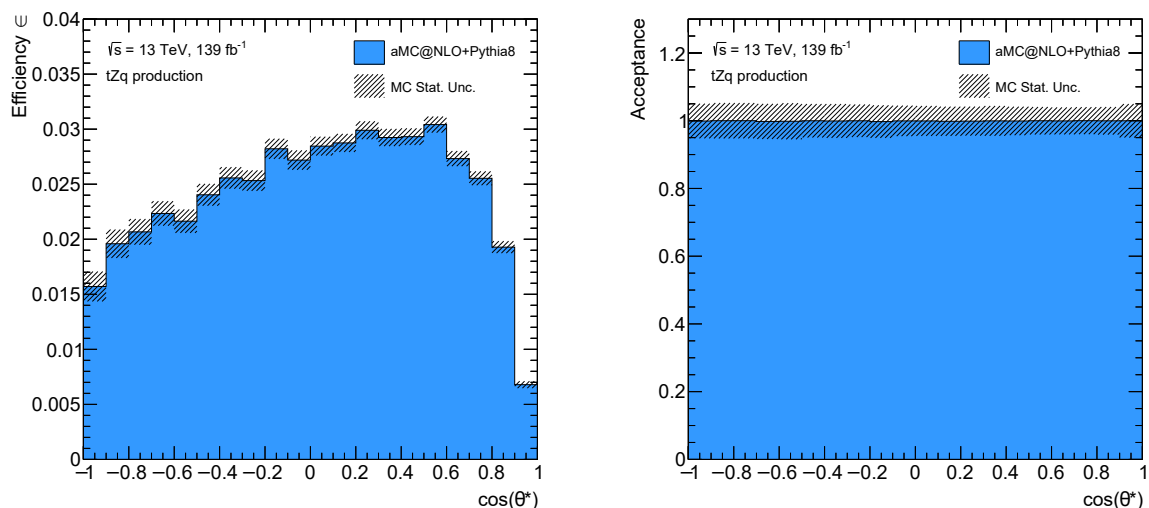

Figure 7.5: (a) Efficiency and (b) Acceptance of $\cos(\theta^*)$ distributions calculated from the differential cross section on truth- and reco-level.

Notably, the efficiency is very low between 1.5% and 3% due to the low number of events in the reconstructed sample. On the reco-level, only 107.66 events make up the distribution while the truth-distribution consists of 4419.76. It is highest in the middle region of the distribution, where the linear behaviour can be best seen in the reconstructed distribution. Towards the high $\cos(\theta^*)$ the efficiency is lowest, fitting the possible rejection through the isolation. As no background samples are investigated in this analysis, the acceptance of the event selection is per definition expected to be 1. Only about 1200 entries in the simulated reco-samples are not matched in the truth-sample, accounting to

negligible variations in the acceptance.

A migration with large off-diagonal elements leads to an unfolding result that can differ strongly from the truth-distribution through enlarged statistical fluctuations [47]. To gain more events per bin and a migration matrix with more events on the diagonal, the bins can be combined to fewer, larger bins. By starting the rebinning from small $\cos(\theta^*)$ and requiring 52% of each line in the migration to be on the diagonal, the migration matrix in Figure 7.6 is found.
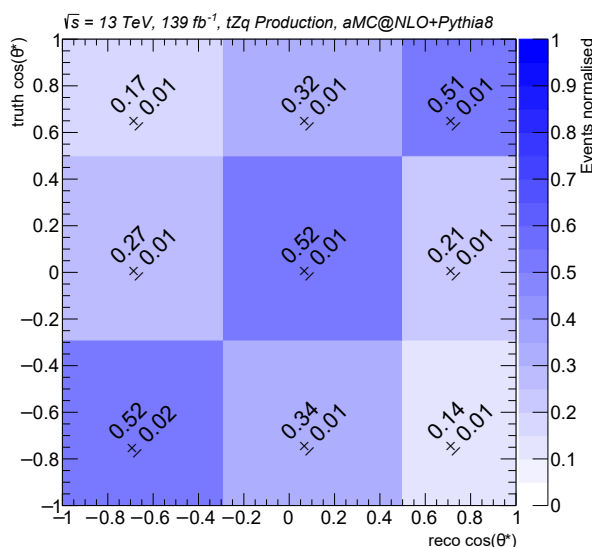

Figure 7.6: Migration of events in tZq production between bins of the $\cos(\theta^*)$ distributions on truth- and reco-level. Each row is normalised to the total event number and is invariant under the migration.

Noticeably, the off-diagonal elements are still large and even the outermost elements contain over 10% of events. This means that, at the current event selection and reconstruction, more than 10% of events with a large angle between the lepton and jet are measured to have these objects close to each other. That can only be explained by using the wrong object from the detector for either the lepton or the jet.

Requiring more events on the diagonal, however, leads to the third diagonal element becoming smaller with less relevance for the distribution until it is negligible and the migration consists of only two elements. Since the behaviour predicted by the SM is linear, at least three bins are necessary, so a discrepancy besides a wrong slope could be noticed. Applying the same binning to the truth- and reco-distributions creates the distributions found in Figure 7.7. Again, the linear behaviour in the truth distribution is easily visible. In the reco-distribution the slope between the first two bins is reduced compared to the truth-distribution corresponding to the nearly constant sector in the fine binned
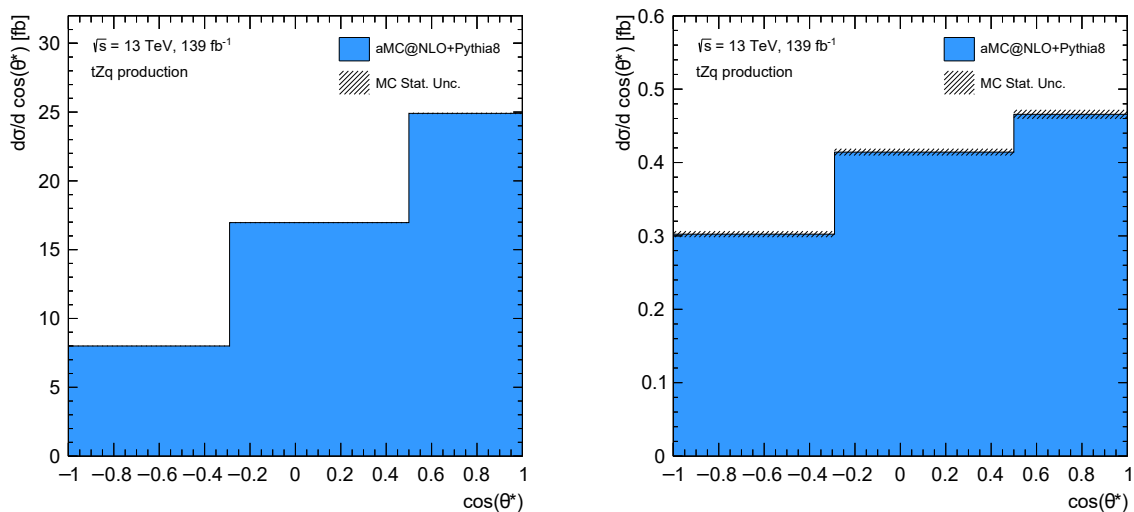
Figure 7.7: Differential cross section with respect to $\cos(\theta^*)$ on (a) truth- and (b) reconstructed level. The distributions are rebinned to match the binning of the migration matrix in Figure 7.6.

reco-distribution. Due to the missing events at high $\cos(\theta^*)$, the last bin is even lower than expected by the slope of the other two bins. The rebinned efficiency and acceptance related to these distributions are shown in Figure 7.8. As before, the efficiency is highest in the middle bins and lower at the edges. The Acceptance is again 1 with negligible variations that are further reduced by averaging multiple bins.
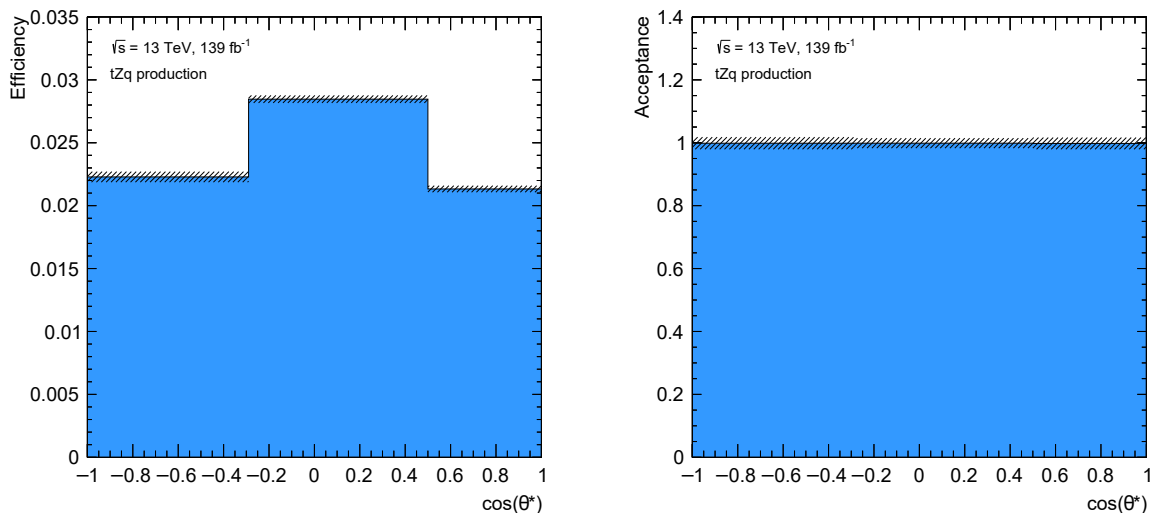
Figure 7.8: (a) Efficiency and (b) Acceptance of $\cos(\theta^*)$ distributions on truth- and reco-level. The distributions are rebinned to match the binning of the migration matrix in Figure 7.6.

7.4 Unfolding

The distributions from the previous section can be used for the profile likelihood unfolding. The unfolded reco-distribution can be seen as data points in Figure 7.9, while the truth-histogram is shown as a red line.
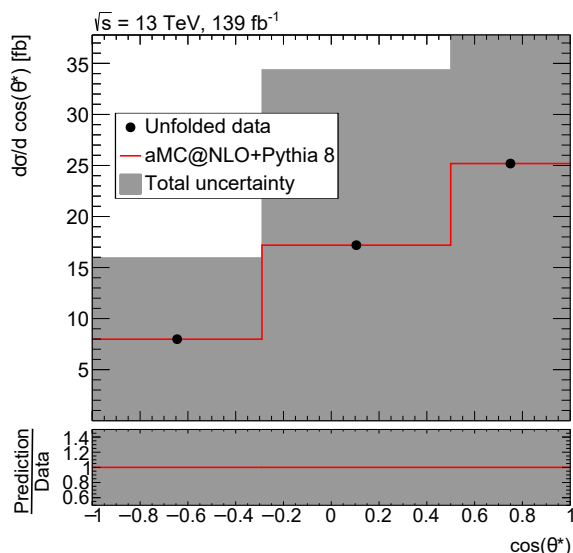

Figure 7.9: Unfolded differential cross section on reco-level as data points compared to truth-level drawn as a red line. The ratio plot shows the ratio between the unfolding result and the truth-distribution, which is exactly one.

Notably, the total uncertainty of the distribution is identical to each bin's value. This means that any one of the bin values could be zero on truth level, which would be compensated by larger values in the other two bins. This large uncertainty shows that a migration with 52% of events on the diagonal is not sufficient to create a meaningful unfolding result with the used profile likelihood unfolding. Since 52% of events being on the diagonal would be expected to be sufficient in general, the problem must occur in the applied unfolding method. As no measured data is unfolded, the reco-distribution is fitted to exactly match the truth-distribution, causing the ratio between the distributions to be exactly one.

Applying a regularisation to reduce the uncertainties leads to the result in Figure 7.10. Since the uncertainty after the regularisation is limited to $\frac{1}{\tau}\frac{\mathrm{d}\sigma}{\mathrm{d}\cos(\theta^*)}$, the shown uncertainties are only a numerical result of the unfolding and do not correspond to an improved description of the studied distribution. Importantly, in this unfolding process the regularisation does not change the bin contents of the distribution. This can be seen from the ratio that, still, is exactly one, which corresponds to the unfolded and truth-distributions being identical.
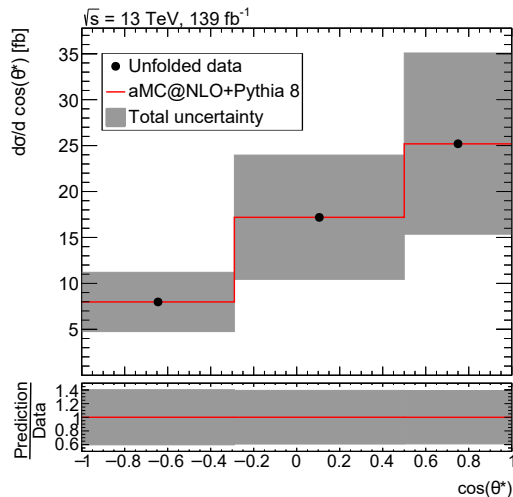
Figure 7.10: Unfolded reco-distribution as data points compared to truth-distribution in red. A regularisation of strength $\tau = 2.5$ is applied. The ratio between the shown distributions is exactly one as without the regularisation.

7.5 Systematic Uncertainties

The studied samples are affected by systematic uncertainties in the object reconstruction. To account for these uncertainties in the Monte Carlo generators, the weights of the entries can be changed. The studied sub-weights are listed in Table 7.2. In total, 102 systematic uncertainties are included in the unfolding. The unfolded distribution with the systematic uncertainties can be seen in Figure 7.11.
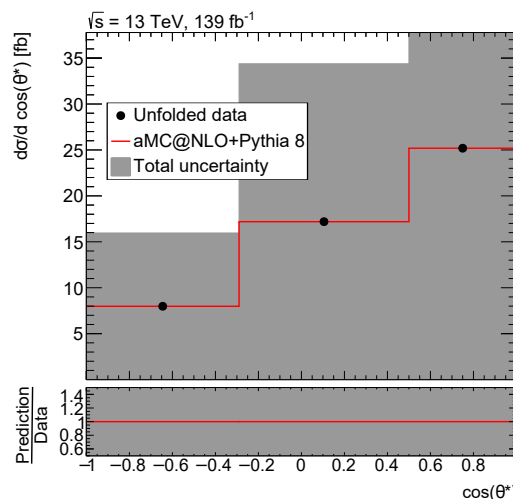

Figure 7.11: Unfolded reco-distribution as data points compared to truth-distribution drawn as a red line. Systematic uncertainties are included in the total uncertainties.

29

As found before, the statistic uncertainties are unexpectedly large, considering the migration matrix. This can again be seen as the total uncertainties are indistinguishable from the statistic uncertainties alone, indicating that the systematic uncertainties are negligible compared to the huge statistic uncertainties.

Weight	Corresponding reconstruction step
`weight_jvt` `weight_forwardjvt` `weight_pileup`	Rejection of jets from pileup in the detector.
`weight_bTagSF_B_X` $(0 \leq \texttt{X} \leq 44)$ `weight_bTagSF_C_X` $(0 \leq \texttt{X} \leq 19)$ `weight_bTagSF_Light_X` $(0 \leq \texttt{X} \leq 19)$	b-tagging of jets with the DL1r neural network based on finding b-, c- and light-jets [42].
`weight_lepSF_EL_RECO` `weight_lepSF_EL_ID` `weight_lepSF_EL_Isol`	Electron reconstruction, identification and isolation.
`weight_lepSF_MU_ID` `weight_lepSF_MU_ID_LOWPT` `weight_lepSF_MU_Isol` `weight_lepSF_MU_TTVA`	Muon identification, isolation and reconstruction by track-to-vertex-association.
`weight_globalTrigger_EL` `weight_globalTrigger_MU`	Triggers applied to detect electrons and muons.

Table 7.2: Weights in the sample affected by systematic uncertainties and the respective object reconstruction in the detector.

7.6 Extraction of Spin Asymmetry

The spin asymmetry that is to be found from the distribution is related to the mean of the observable $\cos(\theta^*)$. By substituting $\cos(\theta^*)$ in equation (2.1) as x and normalising the linear function, the following relation is found:

$$\langle x \rangle = \int_{-1}^{1} x \cdot f(x)\, \mathrm{d}x = \int_{-1}^{1} \left(\frac{1}{2}x + A_t x^2 \right) \mathrm{d}x = \left[\frac{1}{3} A_t x^3 + \frac{1}{4} x^2 \right]_{-1}^{1} = \frac{2}{3} A_t \, . \qquad (7.1)$$

In a histogram with the bin centres b_i, the truth-bin yields N_i, and the signal strengths μ_i, the mean of an observable $\mathcal{O}$ can be computed from these quantities. Rearranging

this formula leads to the first bin's signal strength μ_1 being expressed by the other known parameters and the mean as seen in (7.2).

$$\langle \mathcal{O} \rangle = \frac{\sum_{i=1} b_i N_i \mu_i}{\sum_{i=1} N_i \mu_i} \Leftrightarrow \mu_1 = \frac{\sum_{i=2} (b_i - \langle \mathcal{O} \rangle) N_i \mu_i}{(b_1 - \langle \mathcal{O} \rangle) N_1} \tag{7.2}$$

With this equation, the mean can be found from fitting μ_1 to the distribution. The spin asymmetry can be calculated from the found mean.

By taking the values of two bins as given, a fit in the parameter μ_1 can be performed to find a bin value for the first bin that matches the truth distribution. The result of this fit is shown in Figure 7.12. From the fit, an additional uncertainty of the fit parameter is introduced to the total uncertainty in the first bin leading to even larger uncertainties. The extracted mean is 0.3 ± 1.6 leading to a spin asymmetry of $A_t = 0.45\pm2.4$. Due to the large uncertainties, the full range of possible asymmetries from -1 to 1 is included within one standard deviation of the extracted value. This is consistent with the observation that many different slopes are possible within the uncertainties of Figure 7.9.
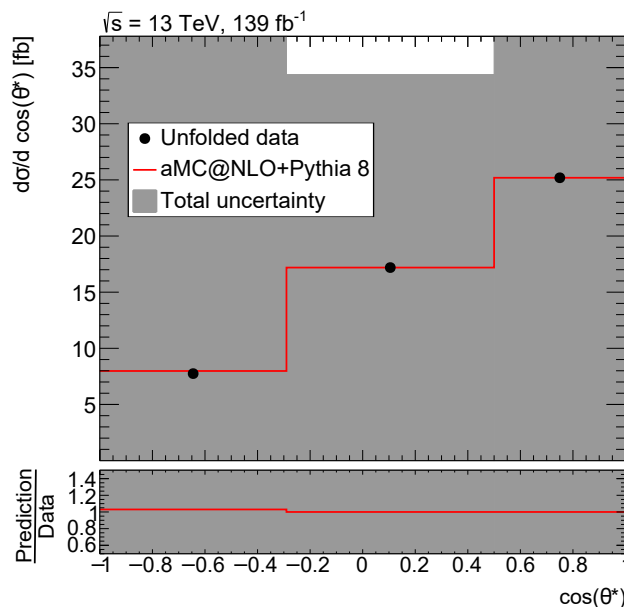

Figure 7.12: Unfolded reco-distribution as data points compared to truth-distribution drawn as a red line. Systematic uncertainties are included in the total uncertainties. The first bin's value is shown as found from a fit, which leads to additional uncertainties of the fit parameter being seen as larger uncertainties. The ratio plot shows a small deviation in the first bin.

The angular correlation α_ℓ of a leptonic top quark decay is 1 at lowest order with a next-to-lowest-order correction of 1×10^{-3} [48]. Using the definition of the spin asymmetry as $A_t = \frac{1}{2} P_t^{(q')} \alpha_\ell$, the top quark's polarisation is found to be 0.9 ± 4.8. While the uncertainty

is still huge, this corresponds to the top quark being polarised along the q' jet in 90% of the events.

8 Conclusion and Outlook

The SM prediction for the spin asymmetry of the top quark in the 4FS is 0.44 [49]. This fits well with the extracted asymmetry of $A = 0.45 \pm 2.4$ in this analysis. However, the uncertainties are larger than the value itself, meaning that the analysis is not sensitive enough to the top quark polarisation, as an asymmetry of $A = 0$ cannot be excluded. The agreement of the extracted value and the SM prediction is expected as only simulated events were used in this thesis. Therefore, this does not show that the SM prediction holds for this observable, but that the extraction was done correctly. However, the large uncertainties suggest that the unfolding procedure from the thesis would not yield an accurate truth-distribution, if applied to measured data.

The top quarks polarisation of 0.9 ± 4.8 also fits recent measurements in single top production via the t-channel without Z boson emission with $P_t^{(q')} = 0.91 \pm 0.10\,(\text{syst.}) \pm 0.02\,(\text{stat.})$ [50]. This fits the prediction that the Z boson radiation in tZq production does not change the top quark's polarisation in the SM.

Further studies could investigate the reconstruction of the top quark and ways of improving it. A good way of finding the source of the inaccuracies would be to compare the W boson on reco- and truth-level by checking if they are within a small ΔR cone of each other. In the case of either the wrong lepton being used for the top reconstruction, or the wrong missing transverse energy being reconstructed in the detector, the W bosons would not be matched. By additionally comparing the top quarks themselves on reco- and truth-level, an inaccuracy coming from the b-jet could be found. As b-jets occur both in top quark and Higgs boson decay, they are very important objects for the research with the ATLAS detector. Thus, they are usually reconstructed with an accurate momentum. However, in the hadronic environment of the ATLAS detector another b-jet could occur and be confused with the b-jet from the top decay. Such a b-jet could stem from the $\bar{b}$ quark produced in the gluon pair production before tZq production as seen in Figure 2.3. To practically improve the reconstruction, some of the following cuts may be helpful:

- A mass constraint for the reconstructed top candidate to be close to the top quark's pole mass

- A minimum value for $E_\mathrm{T}^\mathrm{miss}$ to reduce low-energy backgrounds

- A minimum value for the transverse mass of the top decay's lepton and $E_\mathrm{T}^\mathrm{miss}$ combined

In a further study the respective effects of these cuts could be investigated along with possible additional cuts found from the sources of inaccuracy in the top reconstruction.

Besides necessary improvements of the unfolding, the next step of studying the top quark's polarisation would be to apply the found unfolding process to measured data. With that, the agreement or disagreement between the measurement and the SM can be found to possibly improve our theoretical description of nature.

Bibliography

[1] R. Wideröe, *Über ein neues Prinzip zur Herstellung hoher Spannungen*, Arch. Elektrotech. **21**, 387 (1928)

[2] I. Béjar Alonso, et al., editors, *High-Luminosity Large Hadron Collider (HL-LHC): Technical design report*, CERN Yellow Reports: Monographs, CERN, Geneva (2020)

[3] M. Kobayashi, T. Maskawa, *CP Violation in the Renormalizable Theory of Weak Interaction*, Prog. Theor. Phys. **49**, 652 (1973)

[4] CDF Collaboration, *Observation of top quark production in $\bar{p}p$ collisions*, Phys. Rev. Lett. **74**, 2626 (1995)

[5] DØ Collaboration, *Observation of the top quark*, Phys. Rev. Lett. **74**, 2632 (1995)

[6] S. Weinberg, *The Making of the standard model*, Eur. Phys. J. C **34**, 5 (2004)

[7] A. D. Sakharov, *Violation of CP Invariance, C asymmetry, and baryon asymmetry of the universe*, Pisma Zh. Eksp. Teor. Fiz. **5**, 32 (1967)

[8] S. Hannestad, *Dark energy and dark matter from cosmological observations*, Int. J. Mod. Phys. A **21**, 1938 (2006)

[9] S. L. Glashow, *Partial Symmetries of Weak Interactions*, Nucl. Phys. **22**, 579 (1961)

[10] S. Weinberg, *A Model of Leptons*, Phys. Rev. Lett. **19**, 1264 (1967)

[11] A. Salam, *Weak and Electromagnetic Interactions*, Proceedings of the eighth Nobel symposium **680519**, 367 (1968)

[12] CDF Collaboration, DØ Collaboration, *Combination of CDF and DØ + W-Boson Mass Measurements*, Phys. Rev. D **88**, 052018 (2013)

[13] ALEPH, DELPHI, L3, OPAL, SLD Collaborations, LEP Electroweak Working Group, SLD Electroweak Group, SLD Heavy Flavour Group, *Precision electroweak measurements on the Z resonance*, Phys. Rep. **427**, 257 (2006)

Bibliography

[14] M. Gell-Mann, *A Schematic Model of Baryons and Mesons*, Phys. Lett. **8**, 214 (1964)

[15] H. Fritzsch, M. Gell-Mann, H. Leutwyler, *Advantages of the Color Octet Gluon Picture*, Phys. Lett. B **47**, 365 (1973)

[16] K. G. Wilson, *Confinement of Quarks*, Phys. Rev. D **10**, 2445 (1974)

[17] F. Englert, R. Brout, *Broken Symmetry and the Mass of Gauge Vector Mesons*, Phys. Rev. Lett. **13**, 321 (1964)

[18] P. W. Higgs, *Broken symmetries, massless particles and gauge fields*, Phys. Lett. **12**, 132 (1964)

[19] P. W. Higgs, *Broken Symmetries and the Masses of Gauge Bosons*, Phys. Rev. Lett. **13**, 508 (1964)

[20] G. S. Guralnik, C. R. Hagen, T. W. B. Kibble, *Global Conservation Laws and Massless Particles*, Phys. Rev. Lett. **13**, 585 (1964)

[21] ATLAS, CDF, CMS, DØ Collaborations, *First combination of TEVATRON and LHC measurements of the top-quark mass*, Technical Report ATLAS-CONF-2014-008, CERN, Geneva (2014)

[22] J. Gao, C. S. Li, H. X. Zhu, *Top Quark Decay at Next-to-Next-to Leading Order in QCD*, Phys. Rev. Lett. **110**, 042001 (2013)

[23] Y. Grossman, I. Nachshon, *Hadronization, spin, and lifetimes*, JHEP **07**, 016 (2008)

[24] ATLAS Collaboration, *Observation of the associated production of a top quark and a Z boson in pp collisions at $\sqrt{s} = 13$ TeV with the ATLAS detector*, JHEP **07**, 124 (2020)

[25] CMS Collaboration, *Measurement of the associated production of a single top quark and a Z boson in pp collisions at $\sqrt{s} = 13$ TeV*, Phys. Lett. B **779**, 358 (2018)

[26] CMS Collaboration, *Measurement of the ratio $\mathcal{B}(t \to Wb)/\mathcal{B}(t \to Wq)$ in pp collisions at $\sqrt{s} = 8$ TeV*, Phys. Lett. B **736**, 33 (2014)

[27] ALEPH, DELPHI, L3, OPAL Collaborations, LEP Electroweak Working Group, *A Combination of Preliminary Electroweak Measurements and Constraints on the Standard Model, 2006*, Technical Report CERN-PH-EP-2006-042, CERN, Geneva (2006)

[28] G. Mahlon, S. J. Parke, *Single top quark production at the LHC: Understanding spin*, Phys. Lett. B **476**, 323 (2000)

[29] CMS Collaboration, *Measurement of Top Quark Polarisation in t-channel single top quark production*, JHEP **04**, 073 (2016)

[30] O. S. Bruning, et al., *LHC Design Report Vol.1: The LHC Main Ring*, Technical Report CERN-2004-003, CERN (2004)

[31] ALICE Collaboration, *The ALICE experiment at the CERN LHC*, JINST **3**, S08002 (2008)

[32] ATLAS Collaboration, *The ATLAS Experiment at the CERN Large Hadron Collider*, JINST **3**, S08003 (2008)

[33] CMS Collaboration, *The CMS Experiment at the CERN LHC*, JINST **3**, S08004 (2008)

[34] LHCb Collaboration, *The LHCb Detector at the LHC*, JINST **3**, S08005 (2008)

[35] ATLAS Collaboration, *Operation of the ATLAS trigger system in Run 2*, JINST **15**, P10004 (2020)

[36] ATLAS Collaboration, *ATLAS: Detector and physics performance technical design report. Volume 1*, Technical Report ATLAS-TDR-14, CERN (1999)

[37] T. Sjöstrand, et al., *An introduction to PYTHIA 8.2*, Comput. Phys. Commun. **191**, 159 (2015)

[38] J. Alwall, R. Frederix, et al., *The automated computation of tree-level and next-to-leading order differential cross sections, and their matching to parton shower simulations*, JHEP **07**, 079 (2014)

[39] ATLAS Collaboration, *Electron and photon performance measurements with the ATLAS detector using the 2015-2017 LHC proton-proton collision data*, JINST **14**, P12006 (2019)

[40] ATLAS Collaboration, *Muon reconstruction performance of the ATLAS detector in proton-proton collision data at $\sqrt{s} = 13\ TeV$*, Eur. Phys. J. C **76**, 292 (2016)

[41] M. Cacciari, G. P. Salam, G. Soyez, *The anti-k_t jet clustering algorithm*, JHEP **04**, 063 (2008)

[42] ATLAS Collaboration, *Optimisation and performance studies of the ATLAS b-tagging algorithms for the 2017-18 LHC run*, ATL-PHYS-PUB-2017-013 (2017)

[43] ATLAS Collaboration, *Tagging and suppression of pileup jets with the ATLAS detector*, ATLAS-CONF-2014-018, Geneva (2014)

[44] ATLAS Collaboration, *Forward jet vertex tagging using the particle flow algorithm*, ATL-PHYS-PUB-2019-026, Geneva (2019)

[45] ATLAS Collaboration, *Performance of missing transverse momentum reconstruction with the ATLAS detector using proton-proton collisions at $\sqrt{s} = 13\,TeV$*, Eur. Phys. J. C **78**, 903 (2018)

[46] P. Baroň, J. Kvita, *Extending the Fully Bayesian Unfolding with Regularization Using a Combined Sampling Method*, Symmetry **12** (2020)

[47] V. Blobel, *An Unfolding method for high-energy physics experiments*, in *Conference on Advanced Statistical Techniques in Particle Physics*, pages 258–267 (2002)

[48] A. Czarnecki, M. Jeżabek, J. H. Kühn, *Lepton spectra from decays of polarized top quarks*, Nucl. Phys. **B351**, 70 (1991)

[49] CMS Collaboration, *Inclusive and differential cross section measurements of single top quark production in association with a Z boson in proton-proton collisions at $\sqrt{s} = 13\,TeV$*, JHEP **02**, 107 (2022)

[50] ATLAS Collaboration, *Measurement of the polarisation of single top quarks and antiquarks produced in the t-channel at $\sqrt{s} = 13\,TeV$ and bounds on the tWb dipole operator from the ATLAS experiment*, CERN-EP-2021-263 (2022)

Danksagung

Erklärung nach §13(9) der Prüfungsordnung für den Bachelor-Studiengang Physik und den Master-Studiengang Physik an der Universität Göttingen: Hiermit erkläre ich, dass ich diese Abschlussarbeit selbständig verfasst habe, keine anderen als die angegebenen Quellen und Hilfsmittel benutzt habe und alle Stellen, die wörtlich oder sinngemäß aus veröffentlichten Schriften entnommen wurden, als solche kenntlich gemacht habe.

Darüberhinaus erkläre ich, dass diese Abschlussarbeit nicht, auch nicht auszugsweise, im Rahmen einer nichtbestandenen Prüfung an dieser oder einer anderen Hochschule eingereicht wurde.

Göttingen, den 3. Juli 2022

(Daniel Werner)